Learning wave scattering properties from seismograms

Reza Esfahani[1], Mirko Bracale[1], Léonard Seydoux[2], Michel Campillo[1]

[1]Institut des sciences de la Terre, Université Grenoble Alpes, Grenoble, France
[2]Institut de physique du globe de Paris, UMR CNRS 7154, Université Paris-Cité, Paris, France

Key Points:

- We introduce an unsupervised learning approach to directly evaluate near-source heterogeneity from seismograms
- We propose a proxy termed *local complexity* to quantify near-source structural heterogeneity.
- We demonstrate that our proposed model accurately captures statistical properties of the medium near seismic sources

Corresponding author: R. Esfahani:, `dokhtdor@univ-grenoble-alpes.fr`

Abstract

Heterogeneities in the Earth's crust scatter seismic waves at many scales, trapping seismic energy and producing coda waves that encode valuable information on geological structures. In regions such as volcanoes and fault systems, analyzing coda waves is essential for characterizing non-uniform subsurface heterogeneity, improving interpretation and seismic imaging. Here, we apply unsupervised learning to infer properties directly from seismograms. We simulate 7,800 source-receiver seismograms within a realistic physics-based volcanic model of a magmatic plumbing system with complex interactions between dykes and sills. Recent studies suggest that the spectral characteristics of these synthetic seismograms are controlled by the partial resonance of multiply scattered waves. We leverage a deep scattering transform to extract robust, time-invariant representations of seismograms recorded with multiple stations, and use a manifold learning algorithm to visualize and analyze patterns in the scattering coefficients. By examining the connections in the embedded manifold, we reveal how local medium complexity influences recorded wavefields. Our results demonstrate that the proposed method effectively captures local resonant frequency and modulation induced by heterogeneous structures near the sources. We show that the statistical properties of the medium align with the estimated local complexities derived from seismic signals. By analyzing complete seismograms in a data-driven way, our method enhances subsurface heterogeneity characterization and offers a promising approach for improving the space-time monitoring in highly heterogeneous regions.

Plain Language Summary

The Earth's crust in volcanic and fault zones is made up of a mix of different materials, creating a highly irregular underground structure. Near earthquake and volcanic sources, rock damage and underground fluids amplify certain frequencies in seismic waves, providing insights about subsurface properties. In this study, we introduce a machine learning approach to analyze these signals and reveal underground complexity without needing a large training dataset. Using numerical simulations, we test how well this method can identify different materials and their effects on seismic waves. By recognizing patterns in the data, our approach helps map variations in the subsurface and understand how they influence seismic signatures. Our results show that this technique effectively captures key properties of underground structures and could improve how we monitor earthquakes and volcanic activity over time. While challenges remain in adapting it to different geological settings, this

method offers a promising, data-driven way to study the Earth's interior and track changes in its structure.

1 Introduction

Scattered seismic waves are the results of small-scale heterogeneity in the Earth's crust, generating single and multiple scattering waves called coda waves (Aki & Chouet, 1975). In complex geological environments such as volcanoes and fault systems, seismic wavefields recorded at a surface are mixed with source effects, path effects, and effects of subsurface heterogeneities. Recent studies have shown that in these environments, resonant frequencies are controlled not only by the source but also by the heterogeneous media surrounding it (Ben-Zion & Sammis, 2003; Barajas et al., 2023) (Bracale et al. [xxx]). Identifying the local properties of seismic wavefield in a medium and linking resonant frequencies to local properties can enhance our understanding of geological structures in active regions with high heterogeneity.

Seismic wavefields can be considered a combination of ballistic waves, which propagate straightforwardly, and scattered waves, which follow the ballistic waves and produce the long-lasting coda. The scattered waves consist of combinations of single and multiple scattering arrivals, including conversions between P and S waves. Several approaches have been developed to assess the properties of heterogeneous media in the Earth's interior by analyzing coda regimes in the time-space domain (Aki & Chouet, 1975). First, under single-scattering regime assumption, the coda can be modeled as a superposition of waves scattered once within the medium. However, this oversimplification often fails in cases with strong multiple scattering (e.g. Margerin, 2005; Hennino et al., 2001). As another end-member model, the diffusion model approximates the end part of coda wave energy decay by treating seismic energy as a random walk through the medium (Weaver, 1990; Margerin et al., 2009). To bridge the gap between these two models, Wu and Aki (1988) introduced the radiative transfer equation in seismology to model the decay of energy over time and space. This approach is capable of modeling the seismic energy density in all seismic scattering regimes, including the single scattering, multiple scattering, and diffusive regimes. Nevertheless, it is important to note that these models make use of physically-meaningful quantities, such as the scattering mean free paths (e.g. Margerin, 2005), that can be rigorously defined statistically under the assumption of a uniform distribution of scatterers in the media.

In media with a non-uniform distribution of scatterers, such as volcanic environments, studies have demonstrated a significant contribution of multiply scattered waves with a small mean free path (Del Pezzo et al., 1996; Yamamoto & Sato, 2010a). The high level of heterogeneity can even lead to rapid transition toward diffusion regime, producing spindle-like envelopes with weak P-wave onsets and prolonged coda waves (Yamamoto & Sato, 2010b; Zieger et al., 2016). In addition, it has been suggested that some seismic signatures, like volcanic tremors and long-period earthquakes (B. Chouet, 1992), can have amplified partial resonance frequencies due to damaged and heterogeneous media near sources within the magmatic plumbing system (Barajas et al., 2023), Bracale et al. [xxx].

On the other hand, the ongoing growth in seismic data has empowered applications of machine learning in various tasks in seismology (Mousavi & Beroza, 2022). Machine learning approaches have been used to detect complex patterns in seismic data for tasks such as automated data processing (Mousavi et al., 2020), event detection (e.g. Zhu & Beroza, 2019, with PhaseNet), seismic event localization (Majstorović et al., 2021), seismic denoising (Viens & Van Houtte, 2019), ground-shaking simulation (R. D. Esfahani et al., 2023), exploratory analysis (Mousavi et al., 2019; Seydoux et al., 2020; R. Esfahani et al., 2021), and seismic imaging (Siahkoohi et al., 2022). While most applications of machine learning rely on supervised learning using labeled data, here we employ an unsupervised machine-learning approach to analyze seismograms, extracting robust features to capture resonant frequencies. We utilize a deep scattering transform—a wavelet-based convolutional neural network—to extract robust, time-invariant representations from non-stationary time series (Andén & Mallat, 2014). By using predefined wavelet filters, the deep scattering transform requires no filter learning, making it suitable for small datasets. This approach has been successfully applied to various problems such as music classification (Andén & Mallat, 2014), seismic precursor detection (Seydoux et al., 2020), earthquake clustering (Steinmann, Seydoux, Beaucé, & Campillo, 2022), subsurface monitoring (Steinmann, Seydoux, & Campillo, 2022), and volcano monitoring using continuous seismic records (Steinmann et al., 2024).

The primary objective of this study is to characterize the scattering and elastic properties of a non-uniform heterogeneous medium using unsupervised machine learning. To achieve this, we analyze synthetic seismograms obtained from a companion study by Bracale et al. [xxx] simulated in a 2D realistic magmatic structure based on (Melnik et al., 2021). This model was developed through the injection of dykes and sills into the crust and describes the melt fraction, i.e., the percentage of partially molten material. The effective elastic moduli and seismic velocities are computed using the method proposed by (Schmeling & Wallner, 2012). The wavefield simulation produced 7,800 seismograms recorded at the surface, generated by sources distributed in depth on a regular grid in the central part of the heterogeneous model.

We employ a deep scattering network (DSN) to extract scattering coefficients from synthetic seismograms recorded at multiple stations with two components. We emphasize that the DSN (and the scattering coefficients) in this study differ from the physical scattering of seismic waves, and use the term “coda waves” instead of “scattered waves” to avoid confusion. To analyze and visualize the scattering coefficients, we use a manifold learning algorithm called Uniform Manifold Approximation and Projection (UMAP) (McInnes et al., 2018), a method that embeds the input into a two-dimensional space. Within this embedded space, we perform a local Principal Component Analysis (PCA) on the nearest neighbors of each data point (where each point represents a seismic source) to estimate local complexity and assess local resonant frequencies. The results are consistent with the statistical properties of the medium. We further analyze the effects of polarization of generated seismic S-waves using vertical and horizontal sources on the local complexity analysis. We demonstrate that the proposed technique provides valuable insights into the variations in heterogeneous media.

2 Physics-based simulated training set

The dataset used in this study comes from a companion study that simulates and validates seismic waveforms in a highly heterogeneous medium (Bracale et al. [xxx]). A subregion of the S velocity model is shown in Fig. 1 (the complete velocity model is presented in Fig. S3 in the Supplementary Materials). The model represents a magmatic plumbing system with 10 km sides embedded in a homogeneous medium with flat topography. The average P-wave velocity is $5.5\,\mathrm{km\,s^{-1}}$, and S-wave $3.2\,\mathrm{km\,s^{-1}}$, with a density of $2300\,\mathrm{kg/m^3}$. We adjust the original model by introducing an offset in the minimum S-wave velocity, as the solver employed for the SEM2D simulations solves the elastic wave equation (Komatitsch & Vilotte, 1998; Trinh et al., 2019; Cao et al., 2022). To stabilize the solver, we introduce a minimum value of $200\,\mathrm{m\,s^{-1}}$ in the velocity model.

The velocity model used in this study (subregion of velocity model in Fig. 1 and complete velocity model in Fig. S3) consists of 5,200×3,200 elements with a side length of 5 m, corresponding to a 26×16 km area, to which 4.5 km of absorbing boundaries were added to avoid reflections. The uppermost section of the model contains a homogeneous layer with an approximate thickness of 4 km. Below this depth, we define a heterogeneous shallow zone up to 6 km, containing horizontal structures such as sills. In the deeper part, from 6 to 13 km, the model becomes more heterogeneous due to the presence of vertical dykes. This medium is highly complex, as scattering parameters such as ϵ, which defines the intensity of velocity fluctuations, and the correlation length of the medium (see Supplementary Materials for details, Text S2), exhibit significant variations in space. Therefore, interpreting such data based on scattering theory considerations is extremely challenging, if not impossible, as extensively discussed in Bracale et al. [xxx].

Due to the high computational resources required to run a complete simulation, we take advantage of the reciprocity of the wave equation (Aki & Richards, 2002). This property allows the interchange of source and receiver locations in the source scenario. We then obtain the two components of ground motion generated by 7,800 sources and five receivers by performing only ten numerical simulations. We considered two source mechanisms: a horizontal force and a vertical force, both generated by a Ricker wavelet centered at 3 |hertz. The receivers were placed on the surface, and sources were deployed at depths ranging from 2.5 to 14 km, arranged on a regular grid with a 100 m spacing. The simulated signal duration is 37.4 s.

3 Methods

3.1 Deep scattering transform

Extracting robust representations from seismic waveforms should be tailored to a specific task. The time-frequency domain is particularly suitable for analyzing non-stationary seismograms. The wavelet transform simultaneously decomposes the non-stationary signal into a time-frequency domain, but there is a lack of time-translation invariance. In a deep scattering transform, this invariance is achieved by applying a pooling operation to the scalogram over time. Part of the loss of information due to the pooling operator can be recovered through a second-order wavelet transformation followed by another pooling operator. The pooling operator is user-defined, and acts as a pooling layer in a conventional convolutional neural network (CNN). By cascading wavelet transforms and pooling operations, we use an architecture similar to a convolutional neural network, known as a deep scattering network

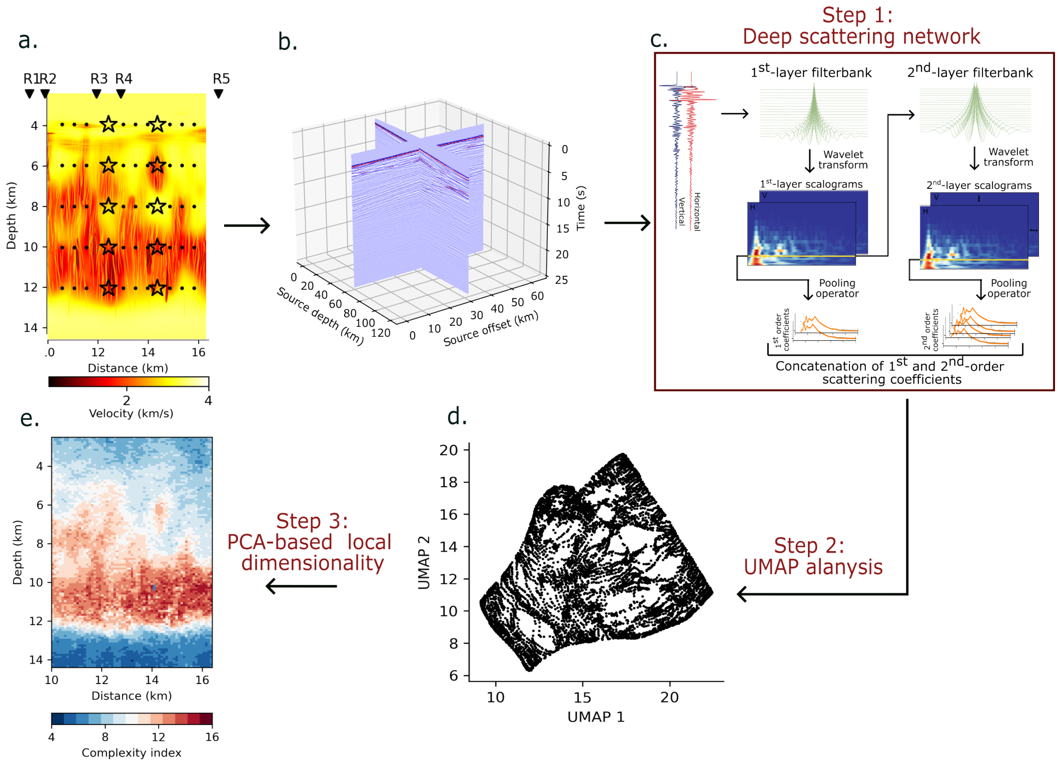

Figure 1. Workflow of the proposed approach. a. Shear wave velocity model used for seismograms simulation in a study by Bracale et al. [xxx]. **b.** Example of seismograms recorded at station R3 for sources at different offsets and depths (8,700 sources). **c.** Step 1: computation of first- and second-order scattering coefficients for a given station and source. **d.** Step 2: representation in the UMAP two-dimensional space. **e.** Step 3: analysis of local complexity in the embedded space using PCA-based local dimensionality.

(DSN, Andén & Mallat, 2014, see Supplementary Materials S1 for the formal details). The architecture is shown in Fig. 1c.

The DSN yields robust, time-translation-invariant representations that retain detailed information from signals in different scales over time and frequency. This architecture has been applied successfully and has outperformed other methods in tasks such as audio and music classification (Andén & Mallat, 2014), seismic signal exploration, and clustering (Steinmann, Seydoux, & Campillo, 2022; Steinmann, Seydoux, Beaucé, & Campillo, 2022; Seydoux et al., 2020).

In DSN, the first layer is defined by applying a wavelet transform to a signal to estimate the first-order scalogram and then the first-order scattering coefficients are calculated by applying a pooling operator. The second-order scalograms are defined by applying the second-order wavelet transforms to the modulus of the first-order scalogram. By applying the pooling operator to the modulus of the second-order scalograms, we calculate the second-order scattering coefficients. The first and second layers of the DSN can have varying numbers of octaves and resolutions. The first-order scattering coefficients capture spectrum-like information (e.g., spectro-temporal energy fluctuations), while the second-order coefficients provide insights into the signal's envelope modulations. Although the architecture of DSN resembles the one of a CNN, it differs in that each layer generates an output, not just the final layer (Andén & Mallat, 2014). Moreover, all filters in the DSN are predefined and not learned from training data. The following explains the details of the parameters used in our implemented DSN and explains how we applied it to seismic data streams.

The pooling operator is key, and must be tailored for specific tasks. Our goal is to analyze the coda waves that follow P- and S-wave onsets, so the pooling operator should mitigate the signature of P- and S-wave arrivals, and emphasize coda waves. Depending on the task, various pooling operators have been employed in seismic data analysis. For earthquake detection, maximum and average pooling operators are commonly used (Seydoux et al., 2020; Steinmann, Seydoux, Beaucé, & Campillo, 2022), while average pooling helped to monitor freezing of the near-surface (Steinmann, Seydoux, & Campillo, 2022). In contrast, the median pooling operator is useful to study the evolution of active volcanic systems over time (Steinmann et al., 2024). The median operator particularly emphasizes background information like coda waves and noise, while minimizing the focus on P- and S-wave arrivals and short-duration events (Steinmann et al., 2024).

Fig. 2a, b presents two synthetic seismograms, one simulated in a high-velocity zone with a local $v_s = 3000\,\mathrm{m\,s^{-1}}$ and subsequently generates less coda waves. The other seismogram is simulated in a dyke with local $v_s = 1000\,\mathrm{m\,s^{-1}}$, which leads to strong coda waves. Fig. 2c, d illustrates the effect of different pooling operators on the first-order scattering coefficients. Compared to the average pooling operator, the median operator more effectively captures information related to coda waves and reduces the influence of P- and S-wave arrivals. The second-order scattering coefficients derived from the median operator (Fig. 2e, f) and the average operator (Fig. 2g, h) demonstrate that the median operator provides better discrimination between seismograms with and without coda waves.

3.2 Uniform Manifold Approximation and Projection (UMAP) analysis

UMAP is a manifold learning technique designed for dimensionality reduction and visualization of high-dimensional data by projecting data onto a low-dimensional embedded space. The UMAP algorithm constructs a manifold that preserves both local and global structures of the data using a graph-based algorithm. This approach focuses on the extraction of the most relevant features from data and is based on algebraic topology and graph theory (more detailes in McInnes et al., 2018). UMAP is scalable and efficient for analyzing large datasets, and is similar to the t-distributed Stochastic Neighbor Embedding (t-SNE, Hinton & Roweis, 2002) and sequencing approaches (Baron & Ménard, 2019; Kim et al., 2020), which are also used for visualizing features and latent spaces in low-dimensional spaces.

UMAP involves three main hyperparameters: the number of nearest neighbors (n_n), the target embedding dimensions (d), and the minimum distance between points in the low-dimensional space (δ). In our case, we set $d = 2$, a common default value. The number of neighbors represents a trade-off between capturing small-scale and large-scale manifold structures. A smaller number of neighbors captures more detailed and localized structures, while a larger number emphasizes global structures but may lose finer details. The δ hyperparameter controls how tightly points are packed in the low-dimensional representation. A smaller δ results in a more densely packed representation that better preserves the local structure, whereas a larger δ spreads out the points, which can aid in visualization. In this study, we use UMAP to visualize high-dimensional scattering coefficients in a two-dimensional space (see Fig. 1c), with a choice of hyperparameters discussed in the Supplementary Materials (Text S3).

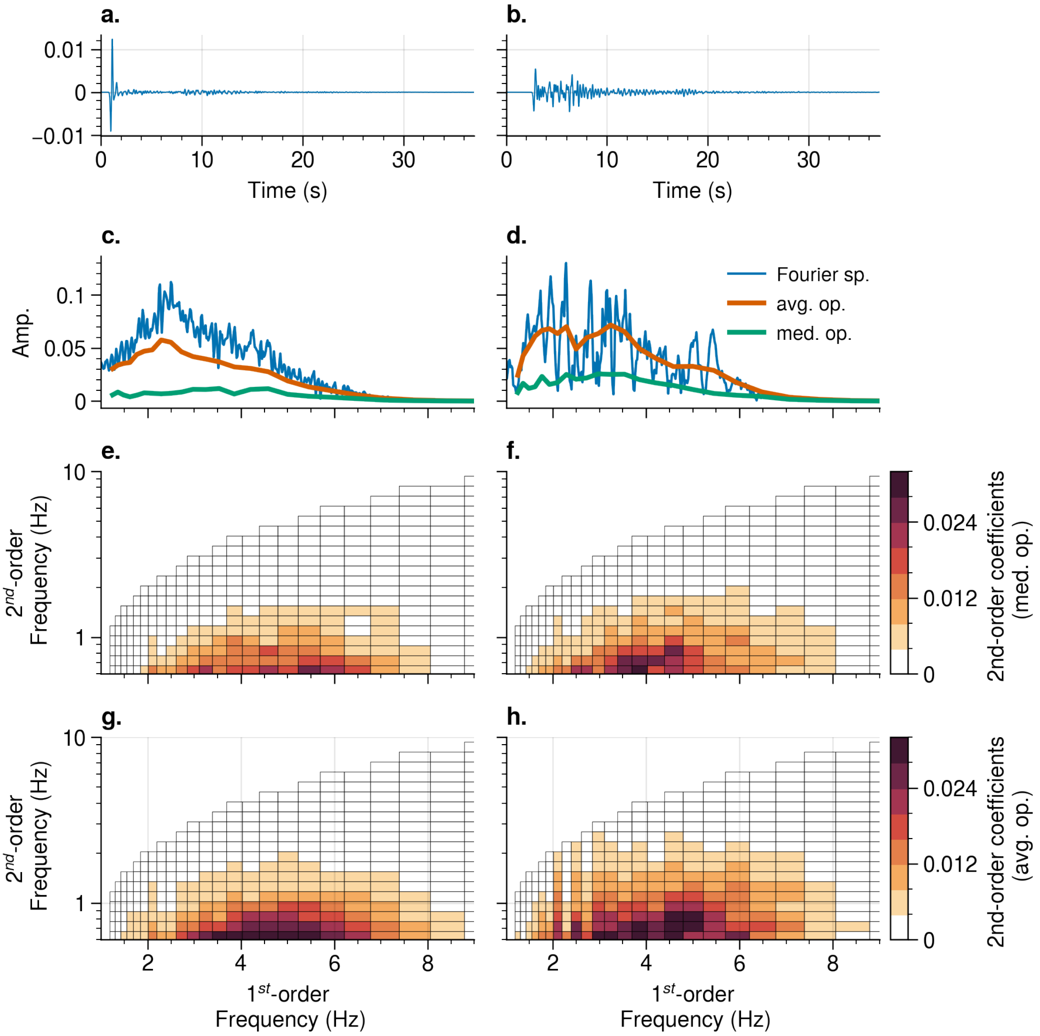

Figure 2. **Effects of pooling operators of DSN on scattering coefficients**. Comparison between median and average pooling operators on two seismograms with sources in (**a.**) high-velocity zone (low codas) and (**b.**) low-velocity zone (strong codas). **c.** **and d.** First-order scattering coefficients based on median (green) and average (red) pooling operators compared with the Fourier spectra (blue). The second-order scattering coefficients based on (**e.** and **f.**) median pooling and (**g.** and **h.**) average pooling operators.

3.3 PCA-based local dimensionality

The balance between local and global structures in UMAP space is achieved through the number of nearest neighbors (n_n). By leveraging the neighboring points of a given data point, we apply a local Principal Component Analysis (PCA) to each point and its n_n surrounding points (see Fig. 1d). We estimate the number of principal components required by performing a local PCA that satisfies a predefined variance threshold, referring to this as local complexity (or local dimensionality). The local complexity shows the embedded dimension of each point and its neighboring points to explain a specific variance (Brodu & Lague, 2012) and was applied to the Fourier representation in (Seydoux et al., 2016) to detect seismic activity from seismic networks. Ideally, the local complexity should align with the embedded dimension of the UMAP space; however, when the local complexity is high, embedding the data in two dimensions becomes challenging for UMAP to learn a manifold in a 2D space. The local complexity is also connected to the local entropy of the seismic wavefield, meaning that higher complexity indicates an increase in coda waves within the wavefield and, as a result increase in entropy. So the local PCA requires more components to explain the wavefield. We emphasize that the PCA-based local dimensionality is directly applied to scattering coefficients, while the UMAP algorithm provides the local connectivity structure via a k-nearest neighbor graph.

In local complexity analysis, the maximum number of principal components is determined by $min(n_n, n_{\text{features}}) - 1$, where n_n is the number of nearest neighbors and n_{features} is the number of scattering coefficients. The minimum number of principal components depends on the parametrization of the UMAP space.

4 Results

4.1 Deep Scattering Representation of Simulated Seismograms

We apply the DSN to the seismograms and extract a robust, time-invariant representations. The implemented DSN consists of two layers. The first layer wavelet bank includes 32 Gabor wavelets with center frequencies ranging from 1.2 to 9 Hz. The second-layer wavelet bank comprises 20 Gabor wavelets with center frequencies between 0.6 and 10 Hz. We use 8 wavelets per octave at the first layer (dense representation) and 5 for the second layer (sparse representation). We use a quality factor of 2 for both layers. The wavelet bank is shown in Fig. S4. For a single station with two channels (horizontal and vertical components), we

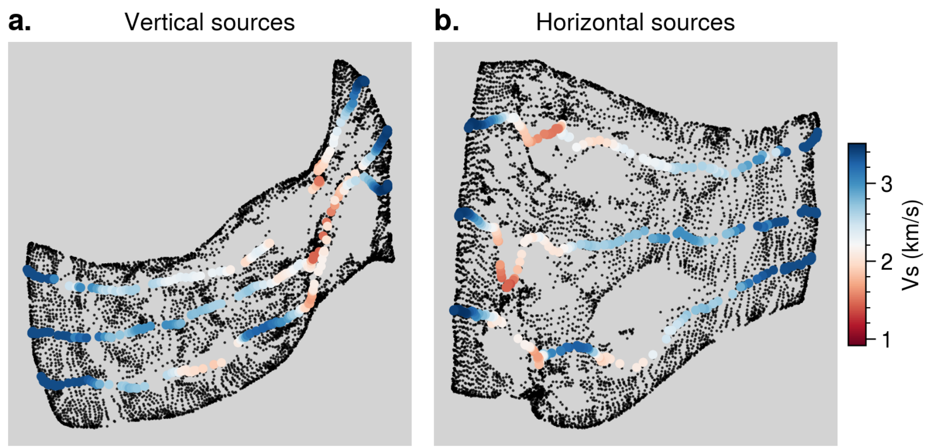

Figure 3. Uniform Manifold Approximation and Projection analysis for **a.** vertical and **b.** horizontal sources. The color represents the average shear-wave velocity surrounding the source locations in vertical segments at distances of 11, 13, and 14.5 km.

obtain 64 scattering coefficients at the first layer and 1,280 at the second. After computing the scattering coefficients, we mask the aliased second-order coefficients with second-order center frequencies above first-order center frequency (following Andén & Mallat, 2014). We analyze vertical and horizontal sources by combining data from all stations, assuming that different stations represent different realizations of the same event. In both cases, the seismograms are normalized before calculating the scattering coefficients. When concatenating data from all stations and all components, the total number of scattering coefficients becomes 320 for the first layer and 6,400 for the second layer. We emphasize that the numbers of scattering coefficients are for records of five stations with two components.

4.2 Scattering coefficients in the UMAP space

Fig. 3 shows the low-dimensional representation from UMAP for vertical and horizontal sources. Each point in the UMAP space corresponds to a source in the subsurface. To better visualize the local and global structures within the UMAP space, we display the shear-wave velocity around each source for three segments at distances of 11, 13, and 14.5 km.

Fig. S5 shows the behavior of the UMAP manifold for vertical sources with different hyperparameters. While the overall structures of the UMAP spaces remain consistent across different parameters, it demonstrates how UMAP alters local and global structures as the

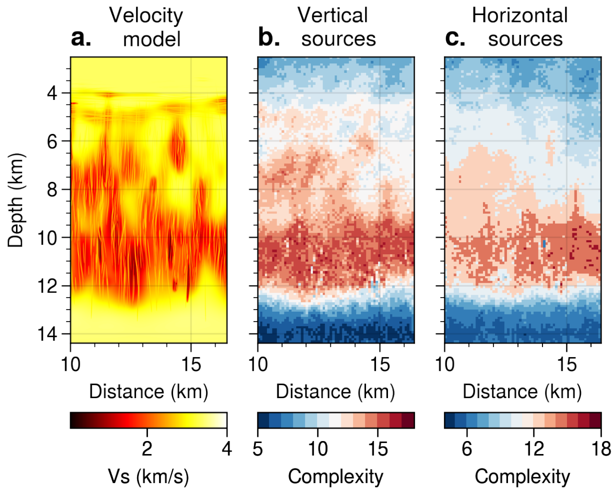

Figure 4. Local complexity analysis. a. Shear wave velocity model. Local complexity for the **b.** vertical sources and **c.** horizontal sources. The PCA explained variance is 80 % for both sources.

number of nearest neighbors changes, especially in low- and high-velocity zones. We test n_n values of 10, 30, and 50 points. As the number of neighbors increases, UMAP tends to group all low-velocity and high-velocity zones at the top and bottom of the model, respectively, aligning with the global structure. We also test δ values of 0.1 and 0.9. Smaller δ values compress the data structure, resulting in more reliable representations. Based on visual inspection, we trade off hyperparameters that preserve both the local and global structures of the data. All analyses in Fig. 3 were performed with consistent hyperparameters: $\delta = 0.1$ and $n_n = 40$ points.

4.3 Local complexity analysis

Our primary goal is to analyze the local structure of the data to characterize subsurface heterogeneities. To achieve this, we evaluate the local complexity using UMAP space with n_n of 20. The results of local PCA are shown in Fig. 4b,c for vertical and horizontal sources, respectively. The results indicate the number of principal components required by local PCA to explain 80 % of the variance of the selected data, based on the local behavior of the UMAP space. The comparison between the local complexity and the velocity model shows that the local PCA captures the details of the velocity model for both sources.

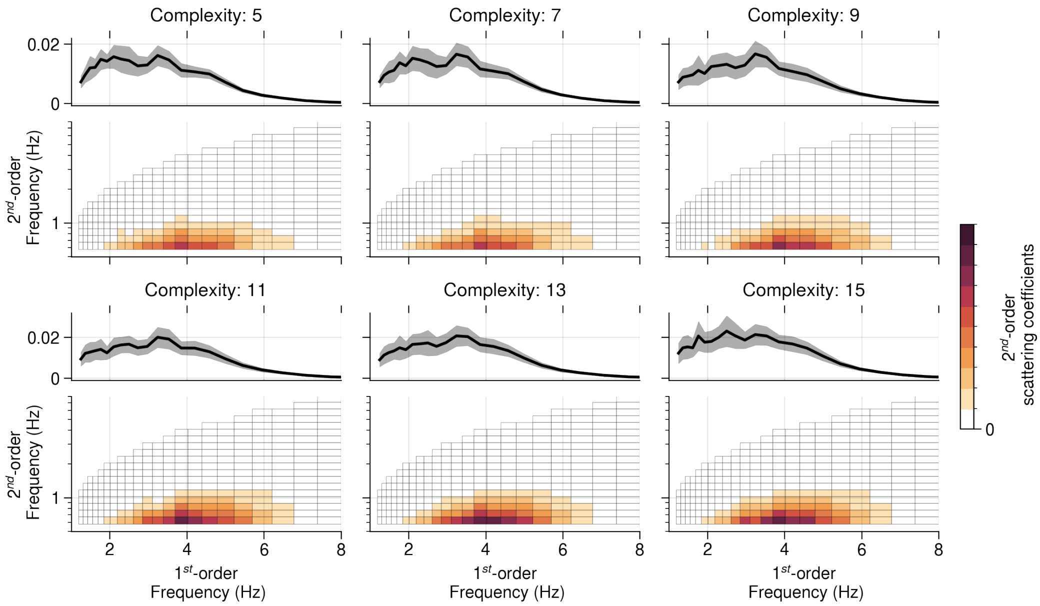

Figure 5. Average scattering coefficients for different complexities. The scattering coefficients are calculated for vertical sources at station R3 (see Fig. 3) and averaged for different values of complexity. The first-order scattering coefficients are shown on the top panels. The black curves show the averaged first-order coefficients and the gray areas show their standard deviations. The second-order scattering coefficients are presented in the bottom panels.

Local complexity analysis in the UMAP manifold is influenced by the number of neighbors and the predefined explained variance. Fig. S5 illustrates the sensitivity of local complexity to these parameters. As the number of neighbors increases, a higher local complexity is required to explain the selected variance. The number of neighbors primarily determines the minimum number of components needed for local PCA analysis. Increasing the explained variance involves more PCA components in the final result, leading to the capture of more details from the scattering coefficients.

Fig. 5 shows the first- and second-order scattering coefficients for different complexity indexes for vertical sources and station R3. It shows that local complexity encodes information about the spectral peaks and frequency modulation. As local complexity increases, it leads to more complex spectral content and a shift toward higher frequencies (observed in the first-order) with larger frequency modulation (second-order).

5 Discussion

Here, we discuss the results of the UMAP analysis and local complexity analysis with a focus on vertical sources. In all of our analyses, we use a seismic network with five stations, as shown in Fig. 1a. The concatenation of records from multiple stations can be different realizations of a source, each affected by a unique path. These effects are mitigated through dimensionality reduction analysis (UMAP) since there is less similarity between them, and leads to accentuating the effects of heterogeneities in the vicinity of sources

5.1 Decoding Subsurface Structures: Interpretation of UMAP Space

UMAP space provides insights into the global and local structures of the scattering coefficients. Fig. 3 shows that the embedded manifold exhibits distinct patterns corresponding to high- and low-velocity zones. Sources in high-velocity zones are more widely distributed, while those in low-velocity zones appear densely embedded. This observation remains valid even by using different UMAP hyperparameters as shown in the Supplementary Materials Fig. S6.

5.2 Relation between Local Complexity and Statistical Properties of the Medium

Fig. 6 shows the relationship between local complexity and the average shear-wave velocity around each source for horizontal and vertical sources. The results indicate that high complexity levels capture low-velocity zones in the medium for both types of sources. This can be interpreted as an increase in entropy in the wavefield related to the seismic wave scattering in the low-velocity zones. As a result, the local PCA requires more components to capture the designated variance. The absolute residual (spectra peak anomaly)of the first layer is estimated between the first-order scattering coefficients for each complexity level and the average across all coefficients in Fig. 6. The results show that in the high-velocity zone between 12 and 14 km, the complexity is lowest, with residuals of scattering coefficients between 1 and 3 Hz. In the high-velocity zone at the top of the model, the residuals of scattering coefficients are about 2 Hz. Finally, in the low-velocity zone, the residuals shift to higher frequencies, around 3 to 5 Hz. Fig. 6c and f shows examples of waveforms for station R3 for each complexity level, as it increases, the coda waves in the waveform become more dominant.

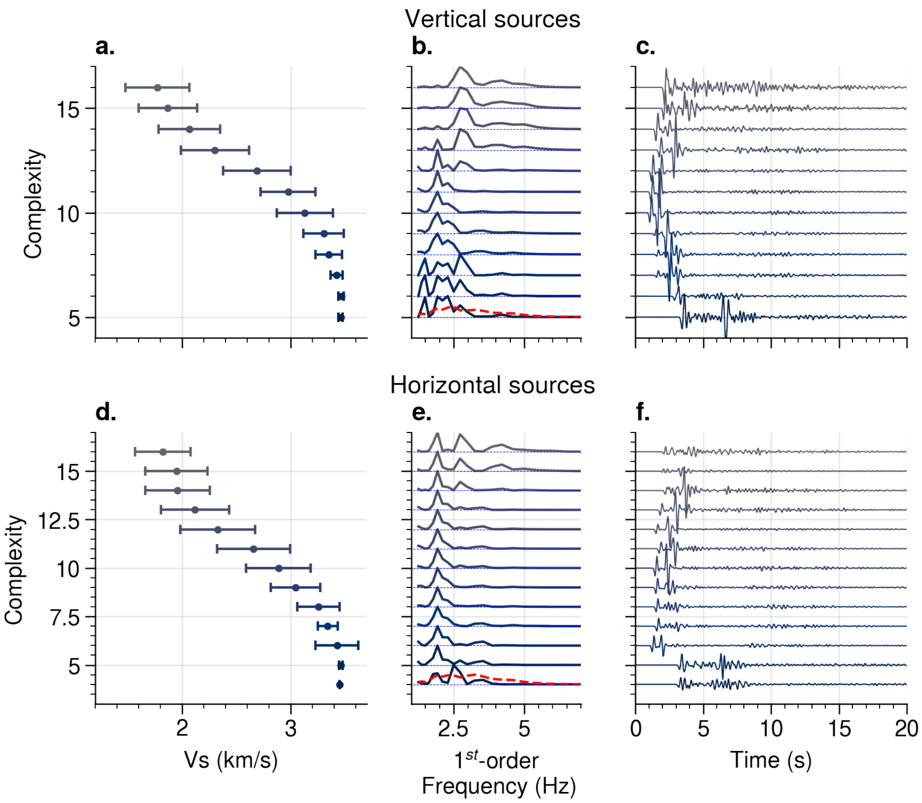

Figure 6. Relationship between complexity analysis and shear-wave velocity. The top panels show results from vertical sources, the bottom ones from horizontal sources. **a., d.** Shear velocity distribution as a function of complexity. **b., e.** First-order coefficients . **c., f.** Examples of vertical components seismograms for each complexities.

Vertical and horizontal seismic sources generate waves with distinct polarizations. A comparison between the local complexity analysis of vertical and horizontal sources in Fig. 4b and c shows that source polarization has marginal effects on the final results. Nevertheless, the result of vertical sources yields better resolution in the top part of the model in depth between 4.5 and 5.5 km compared to the horizontal sources. It is important to note that in real-world scenarios, the polarization of seismic sources is more complex and variable than in this synthetic study, and their effects might be mitigated in the dimensionality reduction step.

The local complexity index captures the statistical properties of the medium as shown in Fig. 7. The correlation length and the intensity of velocity fluctuations ϵ (see Supplementary Materials Text S2) can be considered as a proxy for the mean free path. The correlation

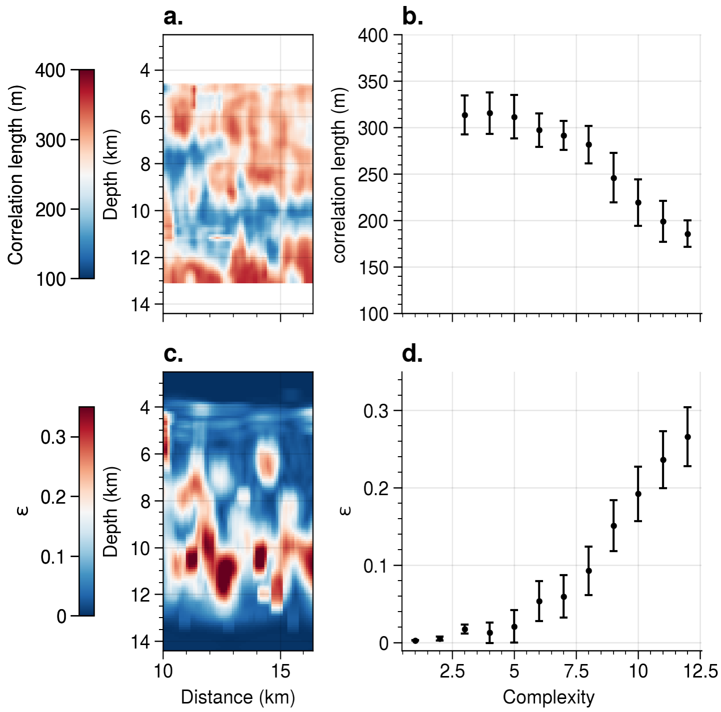

Figure 7. Comparison of medium properties with local complexity. a. Estimated correlation length in the medium. **b.** Relationship between correlation length and local complexity. **c.** Intensity of velocity fluctuations ϵ in space. **d.** Comparison between the intensity of velocity fluctuations and local complexity.

length decreases in the low-velocity regions, indicating that heterogeneities are stronger in these areas. The constant velocity regions at the top and bottom of the model are eliminated here since the velocity is constant. Fig. 7b further demonstrates that as local complexity increases, the properties of the medium change from an elastic to a scattering regime, leading to a decrease in correlation length. Fig. 7c shows the intensity of velocity fluctuations within a 500 m square window, normalized by the average velocity in the window. Higher values of ϵ indicate stronger local heterogeneity. Fig. 7d shows the relationship between the intensity of velocity fluctuations and local complexity and as ϵ increases, the local complexity increases in the model.

It is important to note that in heterogeneous media with a non-uniform distribution of heterogeneity, like the present study, seismic wave scattering regimes are spatially and temporally variable. The mean free path is intertwined with various parameters such as frequency, correlation length, wavenumber, and the intensity of velocity fluctuations. Local complexity can be considered a data-driven proxy for evaluating heterogeneity in the subsurface for such environments.

Given that source locations are required to apply the proposed method, it is also possible to estimate local complexity directly within the spatial domain of the model rather than relying on the combination of the UMAP space and the source locations. We did further analysis applying local complexity using physical locations of sources (grid space with a size of 7×7 around each source, a total of 49 sources) in Fig. S6. The observed local complexities are consistent with results estimated in the UMAP space, suggesting that local complexity behaves similarly across both real location and embedded manifold. It suggests the structure-preserving mapping (isomorphism property) between the embedded domain and the real locations of earthquakes. This is mainly due to the uniform distribution of sources or simplicity in the source mechanism in this study. In real data, earthquakes usually distribute non-uniformly, which can break this property.

5.3 Limitations and outlook for future research

In this work, we have focused solely on synthetic seismic data. However, the proposed method has the potential to be applied to real data in various geological environments. The proposed approach can also help to determine whether spectral peaks in volcanic tremors and low-frequency earthquakes are the result of heterogeneity around the source (Barajas et al., 2023) or due to source processes (B. A. Chouet, 1996).

Various studies have shown the complexity of fault zones using energy entrapment due to significant heterogeneities based on teleseismic records (Share et al., 2017), ambient noise analysis (van Dinther et al., 2020), and the v_P/v_S ratio (Huang et al., 2025). The proposed method can provide insights into the complexity and heterogeneity level of active fault systems by analyzing small earthquakes with accurately determined source locations. We should note that applying the proposed approach to real data faces challenges like the effects of low-velocity and weathering layers near the surface, the influences of topography and the source mechanism.

6 Conclusion

In this study, we propose an unsupervised learning approach to assess heterogeneity in complex geological media directly from seismograms. The proposed method is based on deep scattering transformation and dimensionality reduction techniques. We introduce the complexity analysis as a proxy for the level of heterogeneity and scattering characteristics in media. We show that the complexity of the signal is linked to statistical properties in the vicinity of the source, such as local correlation length and intensity of velocity fluctuations. This approach could have valuable implications for improving the resolution of velocity models and enhancing our understanding of geological structures in active regions, such as fault systems and volcanoes.

Open Research Section

In this paper, we used the Scatseisnet package for deep scattering transformation (Seydoux et al., 2025) and the Scikit-learn package for PCA analysis (Pedregosa et al., 2011). The UMAP algorithm (McInnes et al., 2018) is available in `https://github.com/lmcinnes/umap`. We visualized our results using the Matplotlib (Hunter, 2007) and Proplot (Davis, 2021) packages. The Scipy package is used for other computational analyses (Virtanen et al., 2020). The Python package to reproduce the results in this study is available in the GitHub repository `https://www.github.com/resfahani/scatnet4scatwaves.git/`. The simulated data used in this study is available at `https://zenodo.org/records/15118518`.

Acknowledgments

The authors declare no conflict of interest. This study was supported by the Multidisciplinary Institute in Artificial Intelligence, MIAI, (for R.E., M.C., and L.S.), SPIN (for M.B.), and F-IMAGE (for M.C. and L.S.).

References

Aki, K., & Chouet, B. (1975). Origin of coda waves: source, attenuation, and scattering effects. *Journal of geophysical research*, *80*(23), 3322–3342.

Aki, K., & Richards, P. G. (2002). *Quantitative seismology.*

Andén, J., & Mallat, S. (2014). Deep scattering spectrum. *IEEE Transactions on Signal Processing*, *62*(16), 4114–4128.

Barajas, A., Journeau, C., Obara, K., & Shapiro, N. M. (2023). Comparison of continuously recorded seismic wavefields in tectonic and volcanic environments based on the network covariance matrix. *Journal of Geophysical Research: Solid Earth*, *128*(12), e2023JB026784. Retrieved from `https://agupubs.onlinelibrary.wiley.com/doi/`

abs/10.1029/2023JB026784 (e2023JB026784 2023JB026784) doi: https://doi.org/10.1029/2023JB026784

Baron, D., & Ménard, B. (2019). Black hole mass estimation for active galactic nuclei from a new angle. *Monthly Notices of the Royal Astronomical Society*, *487*(3), 3404–3418.

Ben-Zion, Y., & Sammis, C. G. (2003). Characterization of fault zones. *Pure and applied geophysics*, *160*, 677–715.

Brodu, N., & Lague, D. (2012). 3d terrestrial lidar data classification of complex natural scenes using a multi-scale dimensionality criterion: Applications in geomorphology. *ISPRS journal of photogrammetry and remote sensing*, *68*, 121–134.

Cao, J., Brossier, R., Górszczyk, A., Métivier, L., & Virieux, J. (2022). 3-d multiparameter full-waveform inversion for ocean-bottom seismic data using an efficient fluid–solid coupled spectral-element solver. *Geophysical Journal International*, *229*(1), 671-703. doi: 10.1093/gji/ggab484

Chouet, B. (1992). A seismic model for the source of long-period events and harmonic tremor. In *Volcanic seismology* (pp. 133–156).

Chouet, B. A. (1996). Long-period volcano seismicity: its source and use in eruption forecasting. *Nature*, *380*, 309-316. Retrieved from https://api.semanticscholar.org/CorpusID:4341826

Davis, L. L. B. (2021, October). *Proplot.* Zenodo. Retrieved from https://doi.org/10.5281/zenodo.5602155 doi: 10.5281/zenodo.5602155

Del Pezzo, E., Simini, M., & Ibanez, J. (1996). Separation of intrinsic and scattering q for volcanic areas: a comparison between etna and campi flegrei. *Journal of volcanology and geothermal research*, *70*(3-4), 213–219.

Esfahani, R., Vogel, K., Cotton, F., Ohrnberger, M., Scherbaum, F., & Kriegerowski, M. (2021). Exploring the dimensionality of ground-motion data by applying autoencoder techniques. *Bulletin of the Seismological Society of America*, *111*(3), 1563–1576.

Esfahani, R. D., Cotton, F., Ohrnberger, M., & Scherbaum, F. (2023). Tfcgan: Non-stationary ground-motion simulation in the time–frequency domain using conditional generative adversarial network (cgan) and phase retrieval methods. *Bulletin of the Seismological Society of America*, *113*(1), 453–467.

Hennino, R., Trégourès, N., Shapiro, N., Margerin, L., Campillo, M., Van Tiggelen, B., & Weaver, R. (2001). Observation of equipartition of seismic waves. *Physical review letters*, *86*(15), 3447.

Hinton, G. E., & Roweis, S. (2002). Stochastic neighbor embedding. *Advances in neural information processing systems*, *15*.

Huang, Y., Ide, S., Kato, A., Yoshida, K., Jiang, C., & Zhai, P. (2025). Fault material heterogeneity controls deep interplate earthquakes. *Science Advances*, *11*(9), eadr9353.

Hunter, J. D. (2007). Matplotlib: A 2d graphics environment. *Computing in Science & Engineering*, *9*(3), 90–95. doi: 10.1109/MCSE.2007.55

Kim, D., Lekić, V., Ménard, B., Baron, D., & Taghizadeh-Popp, M. (2020). Sequencing seismograms: A panoptic view of scattering in the core-mantle boundary region. *Science*, *368*(6496), 1223–1228.

Komatitsch, D., & Vilotte, J.-P. (1998, 04). The spectral element method: An efficient tool to simulate the seismic response of 2d and 3d geological structures. *Bulletin of the Seismological Society of America*, *88*(2), 368-392. Retrieved from `https://doi.org/10.1785/BSSA0880020368` doi: 10.1785/BSSA0880020368

Majstorović, J., Giffard-Roisin, S., & Poli, P. (2021). Designing convolutional neural network pipeline for near-fault earthquake catalog extension using single-station waveforms. *Journal of Geophysical Research: Solid Earth*, *126*(7), e2020JB021566.

Margerin, L. (2005). Introduction to radiative transfer of seismic waves. *Geophysical Monograph-American Geophysical Union*, *157*, 229.

Margerin, L., Campillo, M., Van Tiggelen, B., & Hennino, R. (2009). Energy partition of seismic coda waves in layered media: theory and application to pinyon flats observatory. *Geophysical Journal International*, *177*(2), 571–585.

McInnes, L., Healy, J., & Melville, J. (2018). Umap: Uniform manifold approximation and projection for dimension reduction. *arXiv preprint arXiv:1802.03426*.

Melnik, O. E., Utkin, I. S., & Bindeman, I. N. (2021). Magma chamber formation by dike accretion and crustal melting: 2d thermo-compositional model with emphasis on eruptions and implication for zircon records. *Journal of Geophysical Research: Solid Earth*, *126*(12), e2021JB023008. Retrieved from `https://agupubs.onlinelibrary.wiley.com/doi/abs/10.1029/2021JB023008` (e2021JB023008 2021JB023008) doi: https://doi.org/10.1029/2021JB023008

Mousavi, S. M., & Beroza, G. C. (2022). Deep-learning seismology. *Science*, *377*(6607), eabm4470.

Mousavi, S. M., Ellsworth, W. L., Zhu, W., Chuang, L. Y., & Beroza, G. C. (2020). Earthquake transformer—an attentive deep-learning model for simultaneous earthquake detection and phase picking. *Nature communications*, *11*(1), 3952.

Mousavi, S. M., Zhu, W., Ellsworth, W., & Beroza, G. (2019). Unsupervised clustering of seismic signals using deep convolutional autoencoders. *IEEE Geoscience and Remote Sensing Letters*, *16*(11), 1693–1697.

Pedregosa, F., Varoquaux, G., Gramfort, A., Michel, V., Thirion, B., Grisel, O., ... Duchesnay, E. (2011). Scikit-learn: Machine learning in Python. *Journal of Machine Learning Research*, *12*, 2825–2830.

Schmeling, H., & Wallner, H. (2012). Magmatic lithospheric heating and weakening during continental rifting: A simple scaling law, a 2-d thermomechanical rifting model and the east african rift system. *Geochemistry, Geophysics, Geosystems*, *13*(8).

Seydoux, L., Balestriero, R., Poli, P., Hoop, M. d., Campillo, M., & Baraniuk, R. (2020). Clustering earthquake signals and background noises in continuous seismic data with unsupervised deep learning. *Nature communications*, *11*(1), 3972.

Seydoux, L., Shapiro, N. M., de Rosny, J., Brenguier, F., & Landès, M. (2016). Detecting seismic activity with a covariance matrix analysis of data recorded on seismic arrays. *Geophysical Journal International*, *204*(3), 1430–1442.

Seydoux, L., Steinmann, R., Gärtner, M., Tong, F., Esfahani, R., Mouaoued, S., ... Campillo, M. (2025, March). *Scatseisnet, a scattering network for seismic data analysis.* Zenodo. Retrieved from `https://doi.org/10.5281/zenodo.15110686` doi: 10.5281/zenodo.15110686

Share, P.-E., Ben-Zion, Y., Ross, Z. E., Qiu, H., & Vernon, F. L. (2017, 05). Internal structure of the San Jacinto fault zone at Blackburn Saddle from seismic data of a linear array. *Geophysical Journal International*, *210*(2), 819-832. Retrieved from `https://doi.org/10.1093/gji/ggx191` doi: 10.1093/gji/ggx191

Siahkoohi, A., Rizzuti, G., & Herrmann, F. J. (2022). Deep bayesian inference for seismic imaging with tasks. *Geophysics*, *87*(5), S281–S302.

Steinmann, R., Seydoux, L., Beaucé, E., & Campillo, M. (2022). Hierarchical exploration of continuous seismograms with unsupervised learning. *Journal of Geophysical Research: Solid Earth*, *127*(1), e2021JB022455.

Steinmann, R., Seydoux, L., & Campillo, M. (2022). Ai-based unmixing of medium and source signatures from seismograms: Ground freezing patterns. *Geophysical Research Letters*, *49*(15), e2022GL098854.

Steinmann, R., Seydoux, L., Journeau, C., Shapiro, N. M., & Campillo, M. (2024). Machine learning analysis of seismograms reveals a continuous plumbing system evolution beneath the klyuchevskoy volcano in kamchatka, russia. *Journal of Geophysical Research: Solid Earth*, *129*(3), e2023JB027167.

Trinh, P.-T., Brossier, R., Métivier, L., Tavard, L., & Virieux, J. (2019). Efficient time-domain 3d elastic and viscoelastic full-waveform inversion using a spectral-element method on flexible cartesian-based mesh. *GEOPHYSICS*, *84*(1), R61-R83. Retrieved from `https://doi.org/10.1190/geo2018-0059.1` doi: 10.1190/geo2018-0059.1

van Dinther, C., Margerin, L., & Campillo, M. (2020, 12). Laterally varying scattering properties in the North Anatolian Fault Zone from ambient noise cross-correlations. *Geophysical Journal International*, *225*(1), 589-607. Retrieved from `https://doi.org/10.1093/gji/ggaa606` doi: 10.1093/gji/ggaa606

Viens, L., & Van Houtte, C. (2019, 12). Denoising ambient seismic field correlation functions with convolutional autoencoders. *Geophysical Journal International*, *220*(3), 1521-1535. Retrieved from `https://doi.org/10.1093/gji/ggz509` doi: 10.1093/gji/ggz509

Virtanen, P., Gommers, R., Oliphant, T. E., Haberland, M., Reddy, T., Cournapeau, D., ... SciPy 1.0 Contributors (2020). SciPy 1.0: Fundamental Algorithms for Scientific Computing in Python. *Nature Methods*, *17*, 261–272. doi: 10.1038/s41592-019-0686-2

Weaver, R. L. (1990). Diffusivity of ultrasound in polycrystals. *Journal of the Mechanics and Physics of Solids*, *38*(1), 55–86.

Wu, R.-S., & Aki, K. (1988). Multiple scattering and energy transfer of seismic waves—separation of scattering effect from intrinsic attenuation ii. application of the theory to hindu kush region. *Scattering and Attenuations of Seismic Waves, Part I*, 49–80.

Yamamoto, M., & Sato, H. (2010a). Multiple scattering and mode conversion revealed by an active seismic experiment at asama volcano, japan. *Journal of Geophysical Research: Solid Earth*, *115*(B7). Retrieved from `https://agupubs.onlinelibrary.wiley.com/doi/abs/10.1029/2009JB007109` doi: https://doi.org/10.1029/2009JB007109

Yamamoto, M., & Sato, H. (2010b). Multiple scattering and mode conversion revealed by an active seismic experiment at asama volcano, japan. *Journal of Geophysical Research: Solid Earth*, *115*(B7). Retrieved from `https://agupubs.onlinelibrary.wiley.com/doi/abs/10.1029/2009JB007109` doi: https://doi

.org/10.1029/2009JB007109

Zhu, W., & Beroza, G. C. (2019). Phasenet: a deep-neural-network-based seismic arrival-time picking method. *Geophysical Journal International*, *216*(1), 261–273.

Zieger, T., Sens-Schönfelder, C., Ritter, J. R., Lühr, B., & Dahm, T. (2016). P-wave scattering and the distribution of heterogeneity around etna volcano. *Annals of Geophysics*, *59*(4).